

Article

Evaluating the Transient Energy Dissipation in a Centrifugal Impeller under Rotor-Stator Interaction

Ran Tao, Xiaoran Zhao and Zhengwei Wang *

Department of Energy and Power Engineering, Tsinghua University, Beijing 100084, China; randytao@mail.tsinghua.edu.cn (R.T.); zhaoxr14@mails.tsinghua.edu.cn (X.Z.)

* Correspondence: wzw@mail.tsinghua.edu.cn

Received: 20 February 2019; Accepted: 8 March 2019; Published: 11 March 2019



Abstract: In fluid machineries, the flow energy dissipates by transforming into internal energy which performs as the temperature changes. The flow-induced noise is another form that flow energy turns into. These energy dissipations are related to the local flow regime but this is not quantitatively clear. In turbomachineries, the flow regime becomes pulsating and much more complex due to rotor-stator interaction. To quantitatively understand the energy dissipations during rotor-stator interaction, the centrifugal air pump with a vaned diffuser is studied based on total energy modeling, turbulence modeling and acoustic analogy method. The numerical method is verified based on experimental data and applied to further simulation and analysis. The diffuser blade leading-edge site is under the influence of impeller trailing-edge wake. The diffuser channel flow is found periodically fluctuating with separations from the blade convex side. Stall vortex is found on the diffuser blade trailing-edge near outlet. High energy loss coefficient sites are found in the undesirable flow regions above. Flow-induced noise is also high in these sites except in the stall vortex. Frequency analyses show that the impeller blade frequency dominates in the diffuser channel flow except in the outlet stall vortices. These stall vortices keep their own stall frequency which is about 1/5 impeller frequency with high energy loss coefficient but low noise level. Results comparatively prove the energy dissipation mechanism in the centrifugal air pump under rotor-stator interaction. Results also provide the quantitative basis for turbomachinery's loss reduction design.

Keywords: centrifugal impeller; rotor-stator interaction; energy dissipation; entropy production; flow-induced noise

1. Introduction

Energy conversion is a key issue in turbomachinery flow cases. According to the first law of thermodynamics, the total energy of an isolated system is constant. The energy can be transformed from one system to another system but can be neither created nor destroyed. Thus, the energy conversion including heat transfer, mass transfer and force working finally performs as the total energy change [1]. Energy in flowing fluid includes the internal energy, potential energy, kinetic energy and the product of its pressure and volume [2]. In turbomachinery, if the heat exchange between medium and turbomachine body and the mass transfer are ignored, the mechanical energy loss of fluid medium should be equal to the increasing of thermodynamic energy which is the product of the specific heat capacity and temperature [3]. Briefly speaking, the performance of turbomachinery performs as the temperature changes.

In the actual studies of the performance of aerodynamic and hydraulic flow cases, checking the energy dissipation can be helpful to understand the system energy loss. Entropy, which represents the system chaos, were introduced to describe the irreversibility of thermodynamic system [4]. Diaconescu [5] analyzed the heat-insulated flow in pipelines. The relationship between entropy change

and pressure drop was discussed in detail. Esfahani et al. [6] also studied the entropy production in heat-insulated flow in pipelines. The numerical results were verified by comparison with the experimental data. Yoon et al. [7] analyzed the entropy production in different parts of a turbine stage. The energy losses were quantitatively studied and clarified for a better understand. Jia et al. [8] simulated the flow in a highly-loaded turbine. The analysis of entropy production also helped the judgement of energy loss. VanZante et al. [9] used the concept of irreversibility to understand the loss in compressor. Liu et al. [10] simulated and analyzed the irreversibility represented hydraulic loss in a shroudless hydro turbine. Sun et al. [11] also studied the irreversibility in a compressor in different region like tip leakage, wake and vaneless region. Li et al. [12] numerically and experimentally discussed the energy loss in the reversible pump-turbine based on entropy production analysis. These studies above find the energy loss site and intensity. Understanding the energy dissipation would also help the design of turbomachinery by reducing the loss. Kluxen et al. [13] studied the entropy production due to backflow in axial-flow turbine. Soltanmohamadi et al. [14] optimized the turbine based on entropy production analysis. The energy loss was strongly reduced by over 25% in a wide operation range. Zeinalpour et al. [15] introduced the optimization strategy based on the continuous adjoint formulation for designing the turbine cascade. These studies show that entropy production analysis has great meaning in guiding the optimization design of turbomachinery.

Generally, one can connect the flow regime with the energy dissipation through computational fluid dynamics (CFD) simulation methods. The entropy production strongly relates to the undesirable flow structures. However, the entropy production intensity is not clear under strongly transient flow situation especially in the rotating turbomachinery with rotor and stator. Rotor-stator interaction, as a complex issue in turbomachinery flow cases, has received typical studies in the past by both numerical simulation and experiment [16–18]. In this study, the typical centrifugal air pump flow case is studied by CFD simulation under a reduced rotating speed. The transient flow regime and energy loss are comparatively studied by monitoring the velocity vectors, turbulence kinetic energy fields and specific entropy fields. The field of flow-induced noise is also discussed based on the acoustic analogy method to approximately know the energy transition to acoustic energy [19,20]. This study will give a reference to evaluate the energy dissipation in turbomachinery especially considering the rotor-stator interactions.

2. Numerical Methods

2.1. Governing Equations

In this low Mach number air pump case, the fluid medium is treated as incompressible. The thermodynamic effects are taken into consideration in this 3D incompressible viscous turbulent flow. The time-averaged equations [21], known as Reynolds-averaged Navier-Stokes (RANS) equations, are used to decompose the quantities into time-averaged component and fluctuating component. Thus, the continuity equation and momentum equation can be written as:

$$\frac{\partial \bar{u}_i}{\partial x_i} = 0 \quad (1)$$

$$\rho \frac{\partial \bar{u}_i}{\partial t} + \rho \bar{u}_j \frac{\partial \bar{u}_i}{\partial x_j} = \frac{\partial}{\partial x_j} \left(-\bar{p} \delta_{ij} + 2\mu \bar{S}_{ij} - \rho \overline{u'_i u'_j} \right) \quad (2)$$

where u is velocity, t is time, ρ is density, x is coordinate component, δ_{ij} is the is the Kroneker delta, μ is dynamic viscosity. $\bar{\phi}$ and ϕ' are respectively the time-averaged and fluctuating component of arbitrary parameter ϕ . Term $\rho \overline{u'_i u'_j}$ is called the Reynolds stress. \bar{S}_{ij} is the mean rate of strain tensor:

$$\bar{S}_{ij} = \frac{1}{2} \left(\frac{\partial \bar{u}_i}{\partial x_j} + \frac{\partial \bar{u}_j}{\partial x_i} \right) \quad (3)$$

The total energy equation can be written as:

$$\frac{\partial}{\partial t}(\rho h_{tot}) - \frac{\partial p}{\partial t} + \frac{\partial}{\partial x_j}(\rho u_j h_{tot}) = \frac{\partial}{\partial x_j} \left(\lambda_t \frac{\partial T}{\partial x_j} - u_j \overline{h_{sta}} \right) + \frac{\partial}{\partial x_j} \left[u_j \left(2\mu \overline{S_{ij}} - \rho \overline{u'_i u'_j} \right) \right] \quad (4)$$

where T is temperature, h_{sta} is the static enthalpy, h_{tot} is the total enthalpy that $h_{tot} = h_{sta} + u^2/2$, λ_t is the thermal conductivity. Based on these equations above, the hydraulic energy loss, dissipation and transformation to internal energy can be simulated in detail.

2.2. Eddy Viscosity Turbulence Modeling

The RANS equations are not closed after the quantity-decomposition. Therefore, the concept of eddy viscosity is introduced [22] by establishing the relationship between the Reynolds stress $\rho \overline{u'_i u'_j}$ and the eddy viscosity μ_t as:

$$-\rho \overline{u'_i u'_j} = 2\mu_t \overline{S_{ij}} - \frac{2}{3} k \delta_{ij} \quad (5)$$

where k is the turbulence kinetic energy. Thus, eddy viscosity turbulence models can be built to close the RANS equations by modeling the eddy viscosity μ_t based on statistics or experimental verifications.

In this study, the SST (shear stress transport) model which hybrids the standard $k-\varepsilon$ model and Wilcox $k-\omega$ model is applied [23–25]. It has the advantage in treating the high pressure gradient, strong shear flow and the near wall separations. The turbulence kinetic energy k equation and specific dissipation rate ω equation can be specified as:

$$\frac{\partial(\rho k)}{\partial t} + \frac{\partial(\rho u_i k)}{\partial x_i} = P - \frac{\rho k^{3/2}}{l_{k-\omega}} + \frac{\partial}{\partial x_i} \left[(\mu + \sigma_k \mu_t) \frac{\partial k}{\partial x_i} \right] \quad (6)$$

$$\frac{\partial(\rho \omega)}{\partial t} + \frac{\partial(\rho u_i \omega)}{\partial x_i} = C_\omega P - \beta \rho \omega^2 + \frac{\partial}{\partial x_i} \left[(\mu_l + \sigma_\omega \mu_t) \frac{\partial \omega}{\partial x_i} \right] + 2(1 - F_1) \frac{\rho \sigma_\omega}{\omega} \frac{\partial k}{\partial x_i} \frac{\partial \omega}{\partial x_i} \quad (7)$$

where $l_{k-\omega}$ is the turbulence scale which can be expressed as:

$$l_{k-\omega} = k^{1/2} \beta_k \omega \quad (8)$$

and P is the production term, C_ω is the coefficient of the production term, F_1 is the blending function, σ_k , σ_ω and β_k are model constants.

2.3. Acoustic Analogy Method

In this study, the Lighthill acoustic analogy method is also applied based on the turbulent flow modeling. It can apply the near-field of flow-induced noise by predicting sound power level W_A [26]:

$$W_A = \alpha_\varepsilon \rho \varepsilon M_t^5 \quad (9)$$

where α_ε is a constant equal to 0.1, ε is the eddy dissipation rate, M_t is the specific turbulence kinetic energy which can be calculated by:

$$M_t = \frac{\sqrt{2k}}{V_c} \quad (10)$$

where V_c is the sound speed which is 340 m/s in this case. The flow-induced sound power level L_{sp} can be calculated by:

$$L_{sp} = 10 \log_{10} \left(\frac{W_A}{W_{ref}} \right) \quad (11)$$

where W_{ref} is the reference sound power which is 1×10^{-12} W/m³ in this case.

3. Case Description

3.1. Centrifugal Air Pump Model

The studied centrifugal air pump [27] is shown in Figure 1. It has a 7-bladed radial impeller and a 12-bladed radial diffuser. The value and unit of the geometric parameters are listed in Table 1. The performance parameters and fluid medium properties are listed in Table 2. This is a typical turbomachinery study case which illustrate the centrifugal accelerating flow passing through the rotation impeller and stationary vaned diffuser. Based on the simple blade geometry without twisting, the three-dimensional rotor-stator flow case can be simplified into a quasi-two-dimensional case. Thus, many researchers discussed the flow uniformity, jet-wake structure, leading-edge separation and other typical flow characteristics based on this centrifugal pump model [28–31]. The numerical methods by solving RANS turbulent flow with SST $k-\omega$ model are also verified based on this typical pump unit. To describe the flow rate condition, the dimensionless flow rate coefficient C_φ can be expressed as:

$$C_\varphi = \frac{Q}{\pi U_{i2} R_{i2}^2} \quad (12)$$

where Q is flow rate.

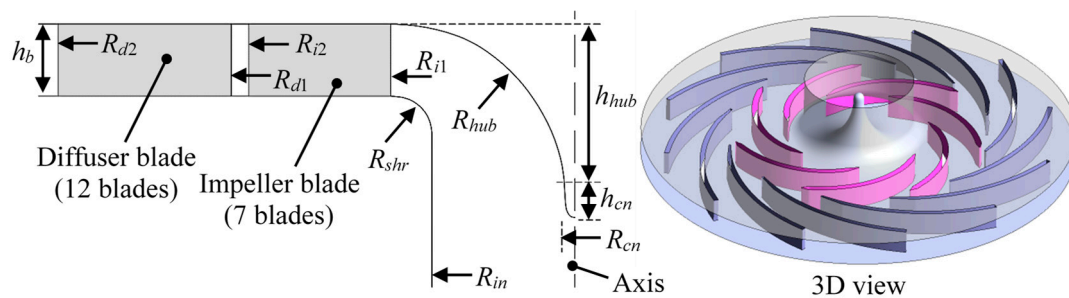


Figure 1. Centrifugal air pump and the indication of its geometric parameters.

Table 1. Geometric parameters of the centrifugal air pump.

Parameter	Value and (Unit)
Impeller blade inlet radius R_{i1}	0.120 (m)
Impeller blade outlet radius R_{i2}	0.210 (m)
Diffuser blade inlet radius R_{d1}	0.222 (m)
Diffuser blade outlet radius R_{d2}	0.332 (m)
Hub arc radius R_{hub}	0.100 (m)
Shroud arc radius R_{shr}	0.025 (m)
Impeller inflow radius R_{in}	0.092 (m)
Cone radius R_{cn}	0.009 (m)
Height of cone h_{cn}	0.026 (m)
Height over cone on hub h_{hub}	0.087 (m)
Height of impeller/diffuser blade h_b	0.020 (m)
Impeller blade number Z_i	7 (-)
Diffuser blade number Z_d	12 (-)

Table 2. Performance parameters and medium properties of the centrifugal air pump.

Parameter	Value and (Unit)
Rotational speed n	2000 (r/min)
Rotational linear speed at impeller outlet U_{i2}	43.98 (m/s)
Flow rate coefficient C_φ	0.048
Fluid medium dynamic viscosity μ	1.83×10^{-5} (kg/m·s)
Fluid medium density ρ	1.2 (kg/m ³)
Fluid medium thermal conductivity λ_t	0.0261 (W/m·K)
Fluid specific heat capacity c_h	1004 (J/kg·K)

3.2. Flow Domain Meshing

The flow domain including the impeller and diffuser should be discretized (meshed) for CFD simulation. In this study, flow domain is meshed by using the commercial software ICEMCFD. The structural mesh is used with hexahedral elements for both the impeller and the diffuser. Two parameters, the specific entropy difference coefficient ΔC_{stot} between impeller inlet and diffuser outlet and the y^+ , are checked to determine the mesh scheme for a better simulation accuracy. The specific entropy difference coefficient ΔC_{stot} can be written as:

$$\Delta C_{stot} = \frac{T_{x2}s_{x2}^* - T_{x1}s_{x1}^*}{2gR_{i2}} \quad (13)$$

where s^* is the specific entropy, g is the acceleration of gravity, subscript x_1 and x_2 denotes two locations. If x_1 is the impeller inflow and x_2 is the diffuser outflow, ΔC_{stot} , in the case that temperature changes slightly, can describe the energy loss in the flow passage from impeller inflow to diffuser outflow by considering $\Delta T \cdot s^*$ instead of $\int T ds$ [32]. Checking ΔC_{stot} can give a better result in predicting the macro energy change in pump. Checking y^+ is to improve the near-wall solution especially in the viscous sub-layer and buffer layer.

In this study, the ΔC_{stot} check is conducted under varying mesh node number from about 2.23×10^5 to about 3.56×10^6 based on the steady state simulation. The residual of C_{stot} is monitored as shown in Figure 2 with the criterion of continually less than 1%. The final mesh is determined with 2,271,260 nodes and 2,073,394 elements in total. The y^+ value is controlled within 7.8~149.3 on both the impeller blades and diffuser blades by setting the first off-wall layer height of 0.03 mm. This y^+ range can be proper for applying the automatic wall treatment [33].

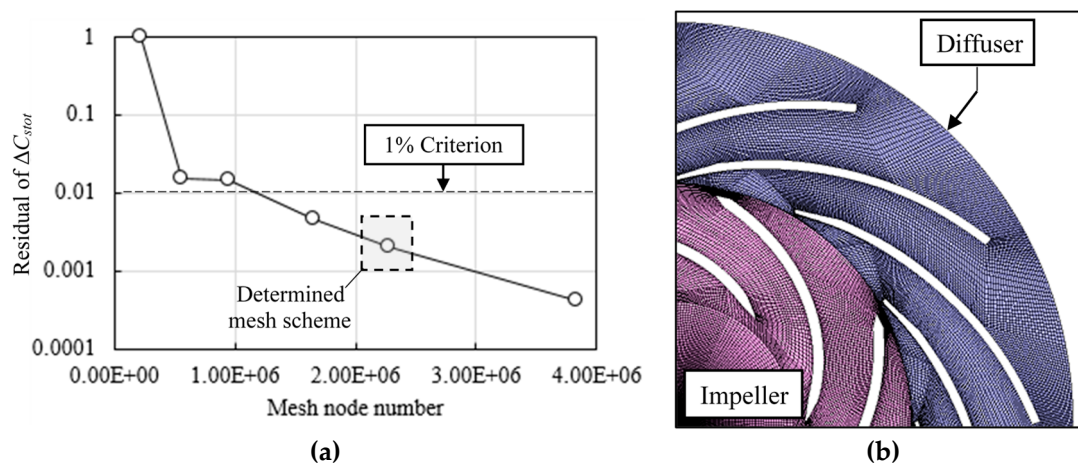


Figure 2. Mesh scheme determination and diagram (a) mesh scheme determination by checking the residual of ΔC_{stot} ; (b) diagram of the mesh scheme.

3.3. Setup of CFD Simulation

In this case, the internal flow in the centrifugal air pump is solved based on Equations (1) to (8) using the finite volume method based on the commercial software ANSYS CFX. The fluid domain used in CFD simulation is shown in Figure 3 based on the numerical methods in Section 2, the fluid medium property in Section 3.1 and the mesh in Section 3.2. The multiple reference frame model is used so that the impeller domain is rotating by $n = 1750$ r/min and the diffuser domain was stationary. Boundary conditions as partially indicated in Figure 3 includes the following parts:

- Velocity inlet: the velocity at inlet boundary, V_{in} , was $V_{in} = Q/A_{in}$ where A_{in} is the impeller inflow area; the temperature at inlet boundary, T_{in} , was 298.15 K; the pressure at inlet boundary, p_{in} , follows the Neumann condition [34]; the inlet turbulence intensity is set as medium of 5%;

- Pressure outlet: the pressure at outlet boundary, p_{out} , was 0 Pa relative to the environment pressure 1 atm; the velocity and temperature at outlet boundary, V_{out} and T_{out} , follows the Neumann condition;
- No slip wall: the impeller hub, impeller shroud, impeller blade, diffuser hub, diffuser shroud and diffuser blade are all in the no slip wall type [35];
- Rotor-Stator interface: an interface is given between impeller and diffuser with conservative interface flux on mass and momentum; the mesh is connected using the general grid interface (GGI) method.

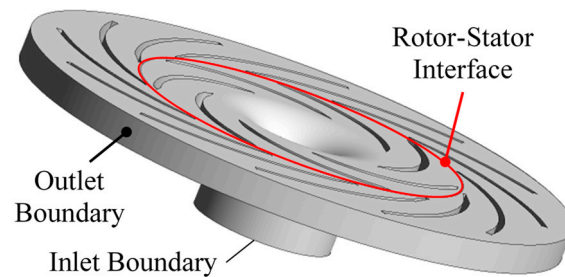


Figure 3. Fluid domain in CFD simulation.

The steady state simulation is conducted as the initial condition. The maximum iteration number is 600 under the criterion of root mean square (RMS) residual less than 1×10^{-5} . The transient simulation is conducted for about 0.343 s (10 impeller revolutions). The time step is 9.52×10^{-5} s with the maximum iteration step number of 10 and the criterion of RMS residual less than 1×10^{-6} . The advection scheme is set as high resolution.

4. Numerical-Experimental Verification Study

To have a reliable numerical result and a better analysis, the numerical-experimental verification is conducted under the original rotational speed of 2000 r/min. The distribution of velocity against U_{i2} is chosen for verification by dividing into radial component C_r and tangential component C_t . Figure 4 shows the comparison between experimental and numerical data by plotting curves. Figure 5 shows the comparison between experimental and numerical data on contours. Parameter G_z is the relative impeller blade channel position where 0~2 means two channels. Parameter S_p is the spanwise position where 0 is at hub and 1 is at shroud.

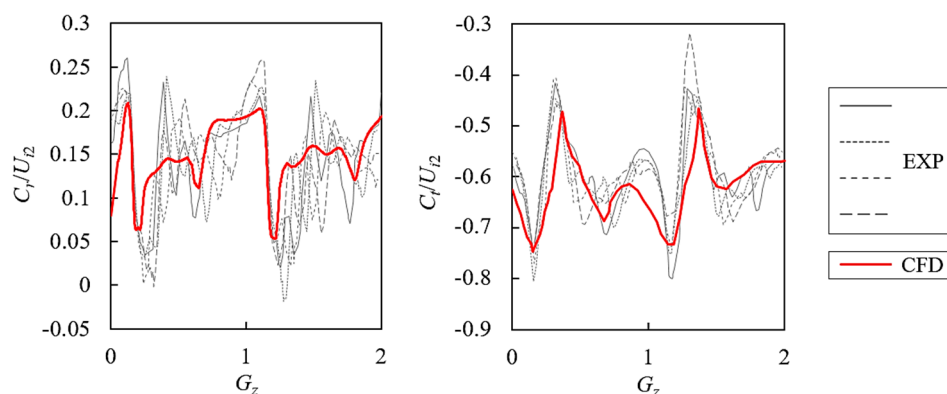


Figure 4. Comparison of the C_r/U_{i2} and C_t/U_{i2} on $R/R_{i2} = 1.02$ and mid-span position within two impeller blade channels. EXP: experimental data at 4 equal-difference acquisition times [27,30]; CFD: numerical data.

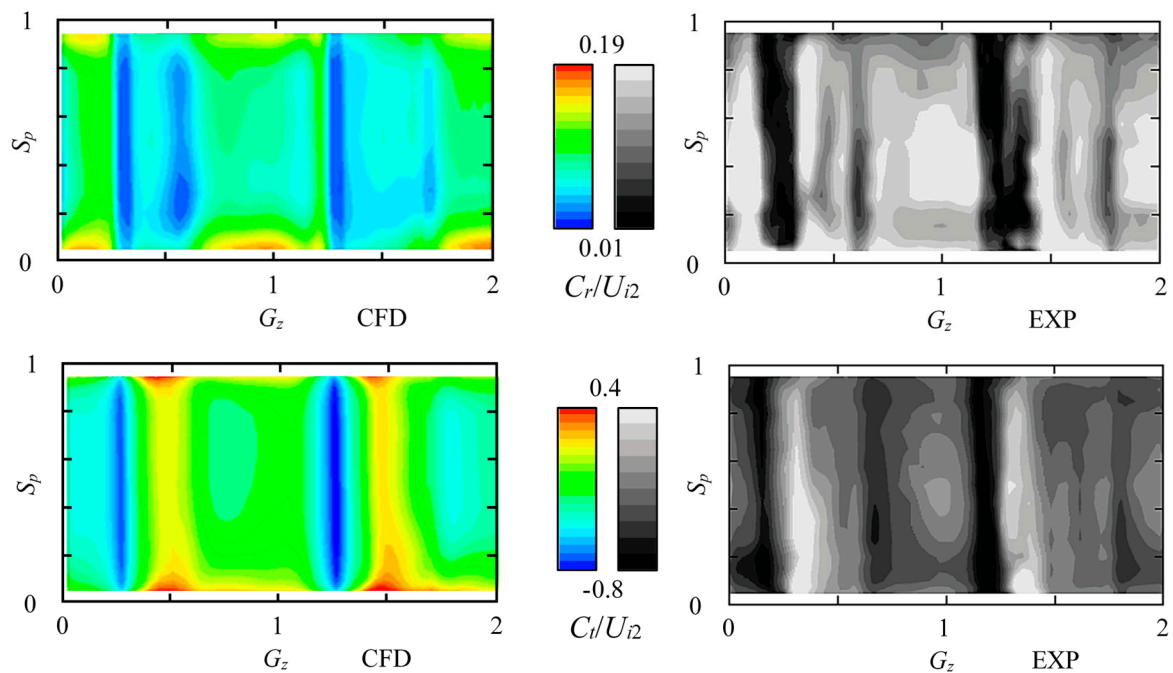


Figure 5. Comparison of the C_r/U_{i2} and C_t/U_{i2} on $R/R_{i2} = 1.02$ circumferential surface within two impeller blade channels. EXP: experimental data [27,30]; CFD: numerical data.

As compared in Figures 4 and 5, the numerical simulation using the RANS method with the SST $k-\omega$ model can predict the similar pattern to the experimental data [27]. In Figure 4, four equal-difference acquisition times are shown. Both the radial velocity component and the tangential component are within the variation range of experimental data. In Figure 5, the high and low velocity sites accord well with the experimental contour. Flow non-uniformity can be observed between the impeller and vaned diffuser. Generally, the numerical simulation is accurate enough to predict the internal flow field and can be used for the energy loss prediction.

5. Transient Flow Field Analysis at Lower-Load

5.1. Velocity Fields

In this study, transient energy loss during rotor-stator interaction is the key issue. Thus, the rotational speed is reduced from original 2000 r/min to 1750 r/min. Based on the reduction, a lower-load situation can be discussed with stronger interaction effects. It can illustrate the transient energy loss happened under the undesirable flow patterns. Based on the settings above, the instantaneous relative velocity contour which indicated the relative flow regime in impeller and diffuser is plotted as shown in Figure 6. The relative velocity coefficient C_{vrel} is defined as:

$$C_{vrel} = \frac{V_{rel}}{U_{i2}} \quad (14)$$

where V_{rel} is the relative velocity.

As indicated in Figure 6, high C_{vrel} region can be mainly found on the suction side of impeller blade and also found near the impeller blade trailing-edge on the pressure side. There are also three mainly low C_{vrel} regions that located at the diffuser outlet, in the impeller trailing-edge wake and near the convex side of diffuser blade. Figure 7 shows the instantaneous flow regime using relative velocity vectors with enlarged views around leading-edges and trailing-edges. A stall vortex flow can be observed in the diffuser outlet low C_{vrel} region. Flow separations are also found on the convex side of the diffuser blade near leading-edge and in the impeller blade's trailing-edge wake. On the contrary, the flow regime is well-behaved near the impeller leading-edge especially on the blade suction side.

Therefore, the low C_{vrel} region is related to the local undesirable flow pattern like separation, wake and vortex. The high C_{vrel} region is because of the smooth local-flow.

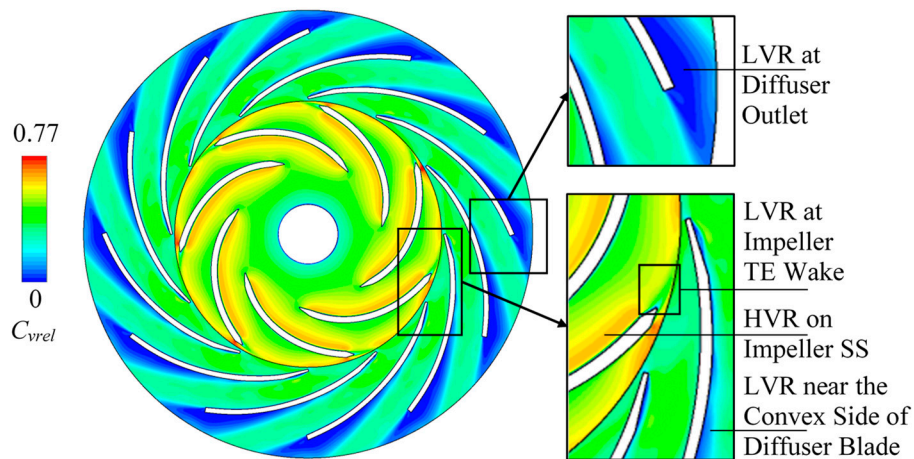


Figure 6. Instantaneous contour of relative velocity coefficient C_{vrel} with indications of the local low and high regions. LVR: low C_{vrel} region; HVR: high C_{vrel} region; SS: blade suction side.

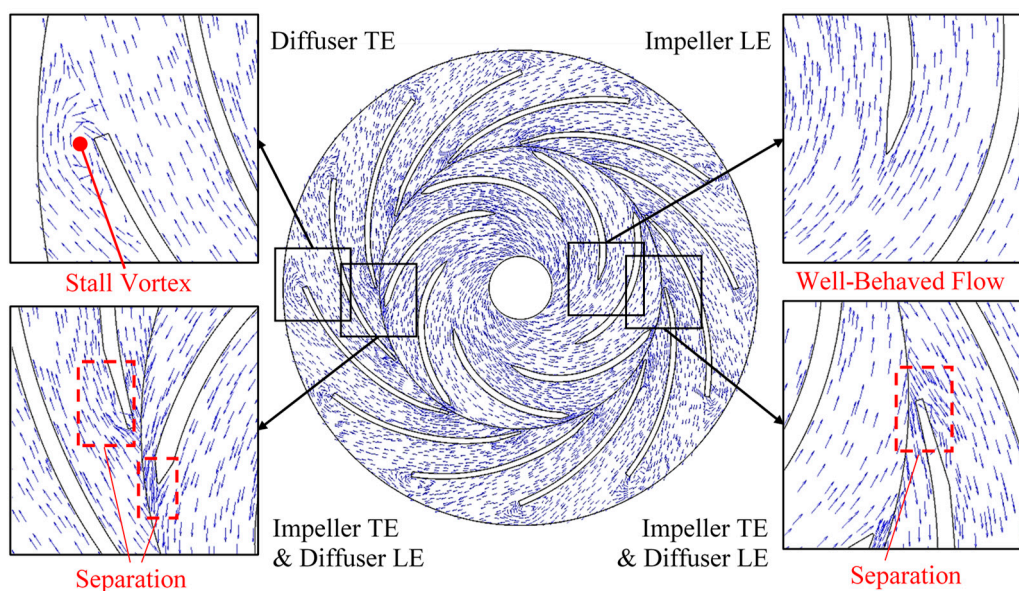


Figure 7. Instantaneous vectors of relative velocity with enlarged views. LE: leading-edge; TE: trailing-edge.

5.2. Energy Dissipation Analysis

The energy dissipation in the centrifugal air pump is analyzed based on the CFD simulation. According to Equation (13), the dimensionless energy dissipation coefficient C_{stot}^* can be defined as:

$$C_{stot}^* = \frac{T \cdot s^*}{2gR_{i2}} \tag{15}$$

The instantaneous C_{stot}^* contour in the impeller and diffuser is shown in Figure 8. The lowest C_{stot}^* region is near the impeller blade leading-edge on the suction side. Three mainly high C_{stot}^* regions can be found at the diffuser outlet, in the impeller trailing-edge wake and near the convex side of diffuser blade. The high C_{stot}^* regions overlap the low C_{vrel} regions as shown in the relative velocity contour map. The low C_{stot}^* regions also overlap the well-behaved flow regions. It revealed that the energy dissipation (transformed to internal energy) is caused by the local undesirable flow regime.

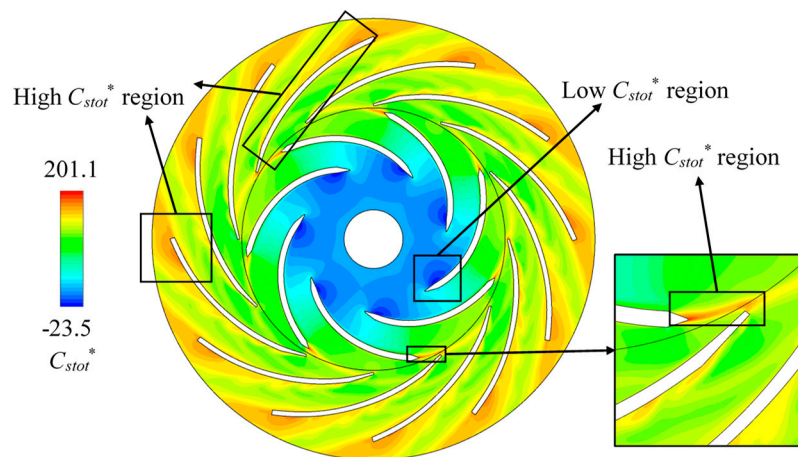


Figure 8. Instantaneous contour of local dissipation coefficient C_{stot}^* with indications of low and high regions.

However, differences can be found in different blade channels. For example, as shown in the enlarged view in Figure 8, the impeller blade trailing-edge wake may cause high C_{stot}^* on the diffuser blade leading-edge. On Figure 6, high C_{stot}^* regions can be obviously found on the leading-edge of 4 of the 12 diffuser blades. The high C_{stot}^* regions on the convex side of the diffuser blade also only occur in some specific channels. These two high C_{stot}^* regions seem to be random or rotationally periodic. To understand this phenomenon and its transient change, the internal flow observation is conducted in the region shown in Figure 9 within one impeller revolution. Monitoring points P_1 to P_4 are also set in the typical high and low C_{stot}^* regions as indicated in Figure 9.

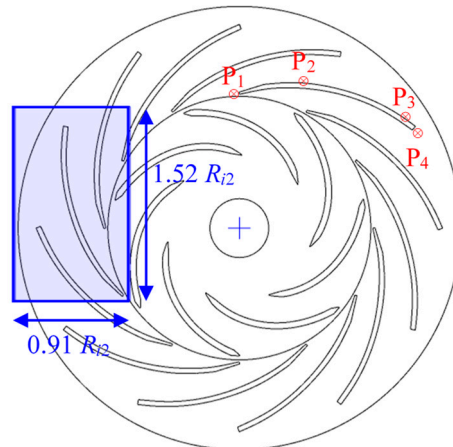


Figure 9. Observation region and monitoring points for the transient pulsation of internal flow characteristics.

Figure 10 shows the C_{stot}^* contour pulsation in one impeller revolution by plotting sub-maps for each $1/18$ revolution. The high C_{stot}^* region consistently exists on the diffuser blade near outlet which is the stall vortex flow site. However, the high C_{stot}^* region in the diffuser trailing-edge wake changed periodically. The high C_{stot}^* regions on the diffuser blade's convex side also periodically generates and disappears. The high C_{stot}^* regions form a street from diffuser blade leading-edge to trailing-edge. Another high C_{stot}^* region occurs periodically on the diffuser leading-edge. Obviously, it is caused by the rotor-stator interaction. When impeller blade trailing-edge wake passes by the diffuser blade leading-edge, high C_{stot}^* generates. The high C_{stot}^* region in the impeller blade trailing-edge wake is relatively stable which consistently exists during impeller rotation.

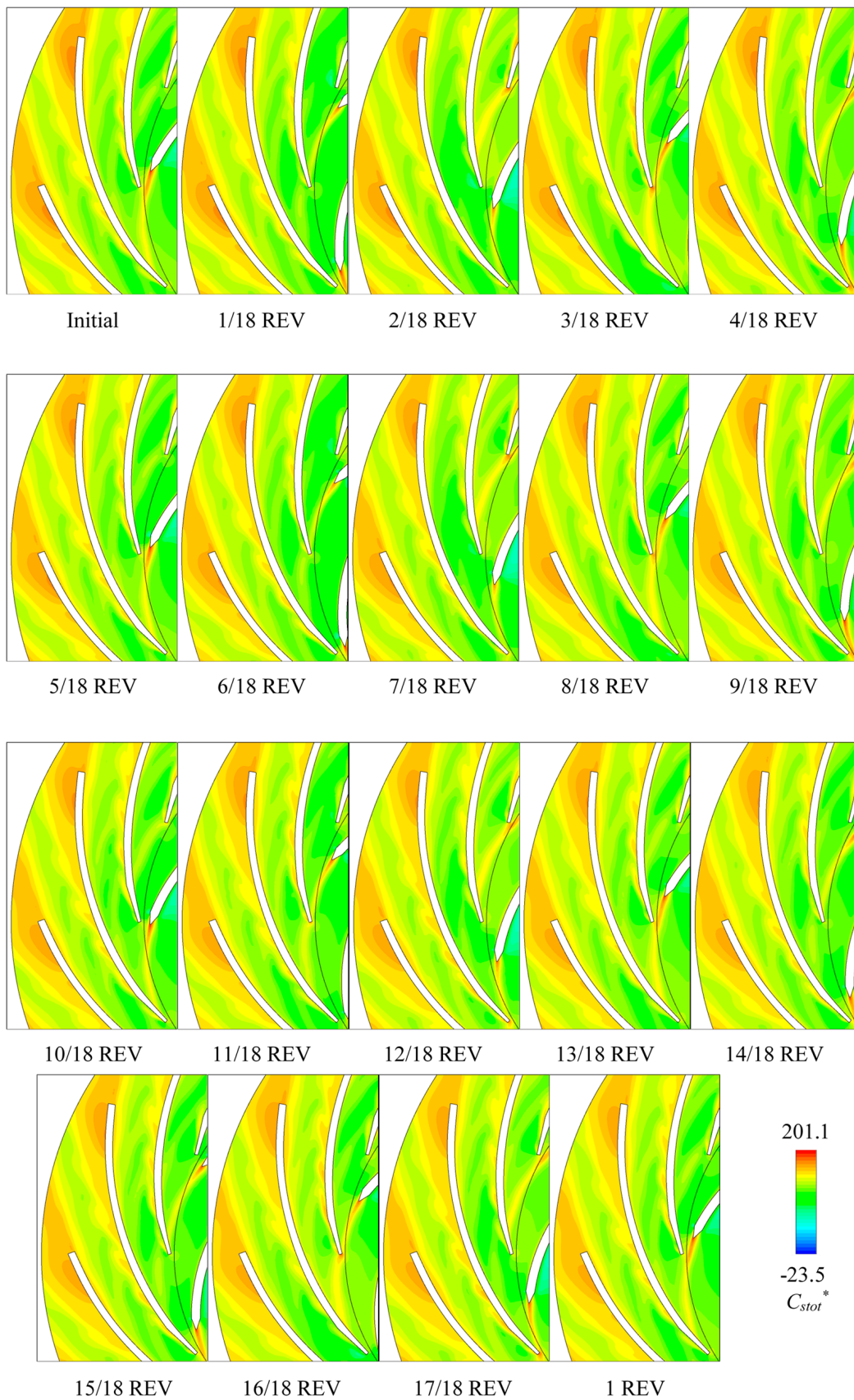


Figure 10. C_{stot}^* contour pulsation in one impeller revolution. REV: impeller revolution.

Based on the monitoring points $P_1 \sim P_4$ shown in Figure 7, the transient C_{stot}^* pulsation is analyzed in frequency in Figure 11. According to the rotating speed of 1750 r/min, the impeller frequency f_{imp} is 29.167 Hz, the impeller blade frequency $f_{ib} = Z_i \cdot f_{imp}$ is 204.167 Hz. Figure 11a is on P_1 which located on diffuser blade leading-edge and is near the impeller blade trailing-edge. The frequency on P_1 is mainly dominated by f_{ib} . The 2-times to 7-times f_{ib} frequencies are also strong. The C_{stot}^* on P_1 seems to be influenced by the rotor-stator interaction. Figure 11b is on P_2 which located on diffuser blade's convex side. The frequency that f_{ib} also dominates and with also 2 to 4 times f_{ib} peaks. The C_{stot}^* on P_2 are also under the rotor-stator interaction. Figure 11c is on P_3 which is in the stall vortex on diffuser blade trailing-edge near outlet. The dominate frequency is a very-low stall frequency f_{TEv} which is about $1/5 f_{imp}$. It is mainly and strongly influenced by the stable stalled vortex structure which is similar as in the rotating stall cases [36,37]. Figure 11d is on P_4 which is in the diffuser blade trailing-edge wake. The frequency on P_4 becomes complex with both the stall frequency f_{TEv} and the 1~4 times of impeller blade frequency f_{ib} . It shows that the C_{stot}^* in diffuser blade trailing-edge wake is influenced by both the impeller incoming flow and the trailing-edge stall vortex flow.

5.3. Turbulence Kinetic Energy Fields

Figure 12 shows the instantaneous contour of turbulence kinetic energy. The turbulence kinetic energy coefficient C_k is defined for analysis:

$$C_k = \frac{k}{2gR_{i2}} \quad (16)$$

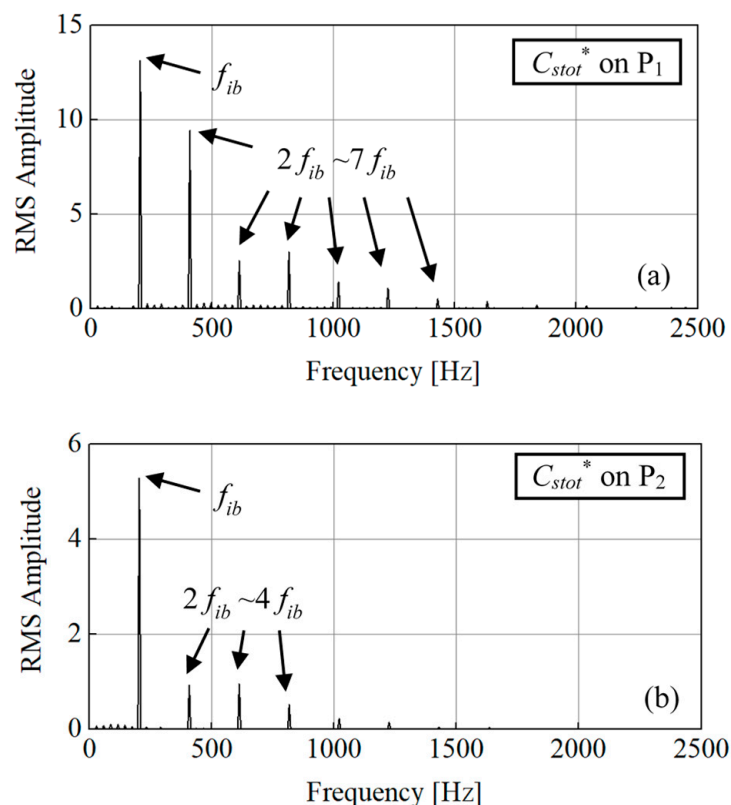


Figure 11. Cont.

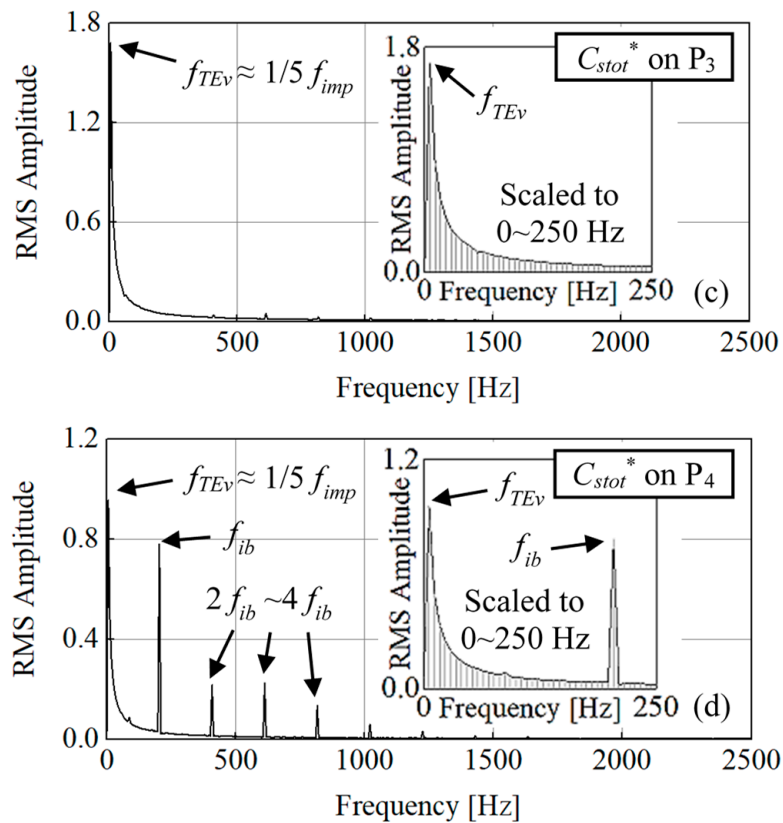


Figure 11. C_{stot}^* pulsation on P_1 , P_2 , P_3 and P_4 within one impeller revolution. (a) on P_1 ; (b) on P_2 ; (c) on P_3 ; (d) on P_4 .

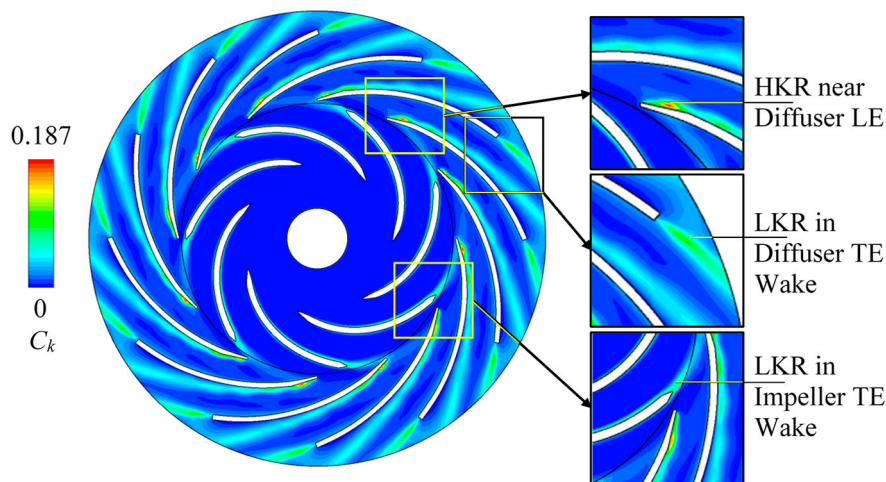


Figure 12. Instantaneous contour of turbulence kinetic energy coefficient C_k with the indications of local low and high regions. HKR: high k region; LKR: low k region; LE: leading-edge; TE: trailing-edge.

The high C_k region mainly occurs on the convex side of diffuser blade, in the diffuser blade trailing-edge wake and in the impeller blade trailing-edge wake. These three regions overlap the high C_{stot}^* regions in Figure 8. However, the stall vortex flow site on diffuser blade near outlet is the low C_k region. It does not accord with the local high C_{stot}^* characteristic.

In Figure 12, the pattern is not symmetric among the channels. The rotor-stator interaction especially the impeller blade trailing-edge wake influences the C_k values at diffuser inlet.

5.4. Flow Induced Noise

The flow induced noise can somehow indicate the extra acoustic energy dissipation. According to Equations (9)–(11), the flow induced noise is strongly related to the turbulence kinetic energy k and turbulence eddy dissipation rate ϵ . Therefore, the flow-induced sound power level L_{sp} is analyzed as the instantaneous contour in Figure 13. The high L_{sp} regions completely accord with the high C_k regions and are obviously stronger than the surrounded low L_{sp} sites. To understand the L_{sp} pulsation during impeller rotation, the L_{sp} contour is monitored and analyzed within one impeller revolution.

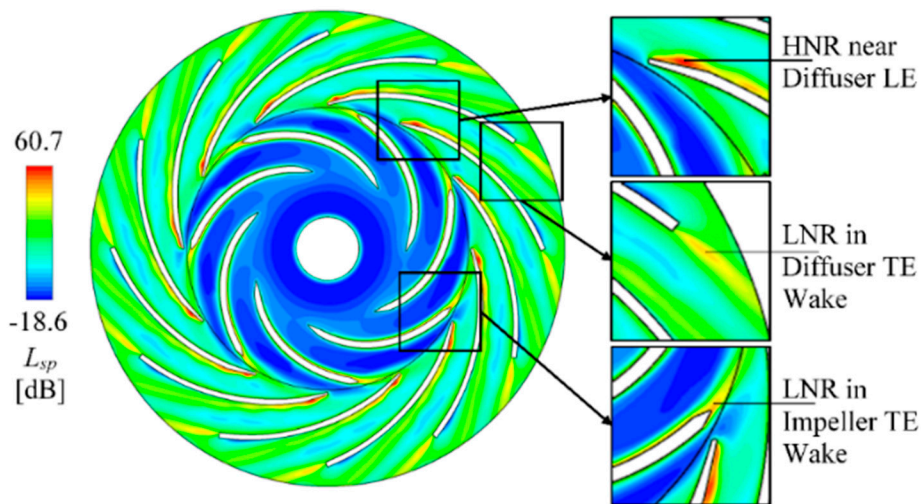


Figure 13. Instantaneous contour of flow-induced noise level L_{sp} with the indications of local low and high regions. HNR: high noise region; LNR: low noise region; LE: leading-edge; TE: trailing-edge.

Figure 14 shows the sub-maps for each 1/18 revolution for the transient L_{sp} fields. The high L_{sp} regions on diffuser blade are no more a street but are triggered from leading-edge and separate into mid-channel. The diffuser leading-edge high and low L_{sp} regions are pulsating due to rotor-stator interaction. The stall vortex region on the diffuser blade near outlet is always low in L_{sp} intensity. The high L_{sp} regions in the impeller blade trailing-edge wake and in the diffuser blade trailing-edge wake always exist and are relatively stable.

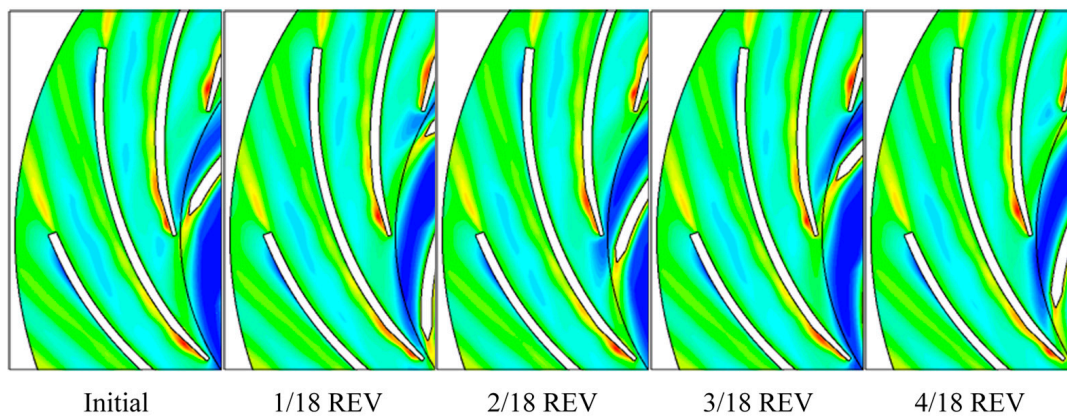


Figure 14. Cont.

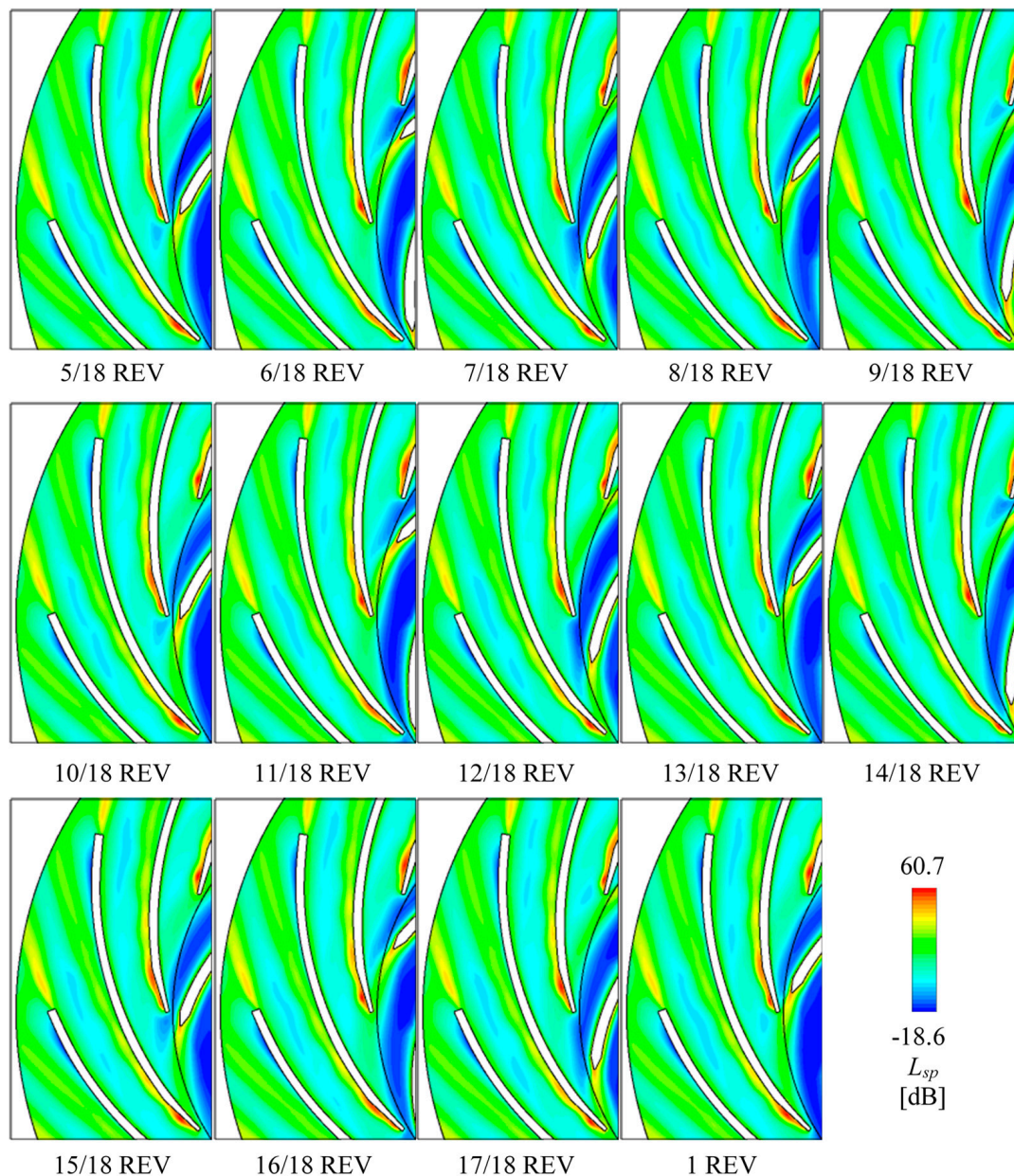


Figure 14. L_{sp} contour pulsation in one impeller revolution. REV: impeller revolution.

Based on the monitoring points $P_1 \sim P_4$ shown in Figure 7, the transient L_{sp} pulsation is analyzed in frequency in Figure 15. Figure 15a is on P_1 . The frequency on P_1 is also mainly dominated by f_{ib} which is the same as the C_{stot}^* pulsation. The 2-times and 3-times f_{ib} frequencies are also strong, which indicate the rotor-stator interaction effect on L_{sp} on P_1 . Figure 15b is on P_2 . The frequency f_{ib} is the only dominate frequency greater than other values. The flow-induced noise field on P_2 is also under the rotor-stator interaction. Figure 15c is on P_3 . The stall frequency $f_{TEv} \approx 1/5 f_{imp}$ is the strongest frequency. The 2 and 3 times f_{imp} are also obvious as peaks. Both the stall frequency and impeller frequency can be found on the L_{sp} on P_3 but the stall frequency dominates. Figure 15d is on P_4 . The L_{sp} pulsation frequency on P_4 is not the same as the C_{stot}^* pulsation frequency. Due to the strong trailing-edge wake, the stall frequency of L_{sp} caused by trailing-edge stall vortex does not strongly impact the local flow. Thus, frequency $f_{TEv} \approx 1/5 f_{imp}$ is not found on Figure 15d but the f_{ib} frequency dominates. The flow induced-noise in the trailing-edge wake is mainly influenced by impeller incoming flow.

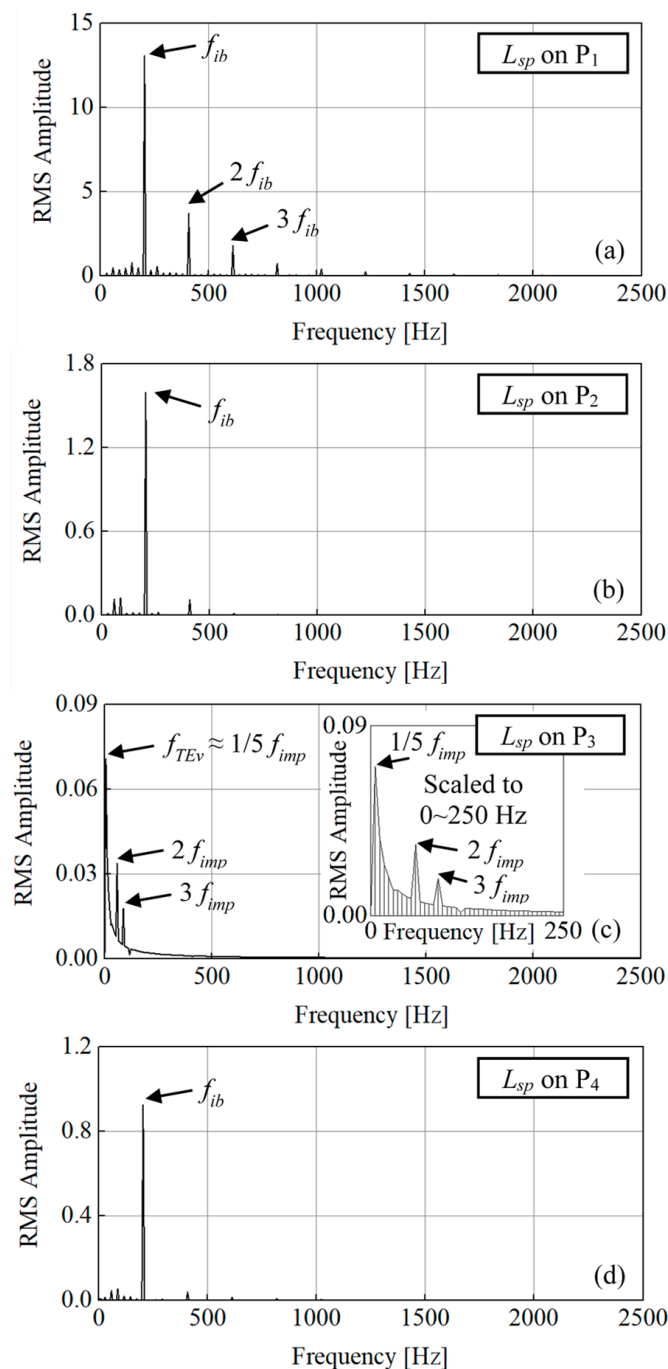


Figure 15. L_{sp} pulsation on P_1 , P_2 , P_3 and P_4 within one impeller revolution. (a) on P_1 ; (b) on P_2 ; (c) on P_3 ; (d) on P_4 .

6. Conclusions

By simulating and analyzing the energy dissipation in centrifugal air pump under rotor-stator interaction, conclusions can be drawn as follows:

- (1) The temperature and static entropy patterns can be successfully found by applying the total energy governing equations. The flow energy which transferred to internal energy can be quantitatively known. The flow-induced noise, which might be another energy dissipation source, can be also predicted based on the turbulence flow modeling. It is found strongly relative to the turbulence kinetic energy and dissipation rate.

- (2) The high static entropy sites are related to the local low velocity regions. According to the vectors of relative velocity, these low velocity regions have undesirable flow regime. The main high static entropy sites locate in the impeller trailing-edge wake, on the diffuser blade leading-edge and convex side, in the diffuser blade trailing-edge stall vortex near outlet and in the diffuser blade trailing-edge wake. The high noise sites overlap some of the high static entropy sites. These overlapped noisy sites are also due to the local undesirable flow regime. There is an exception as stall vortex near diffuser blade trailing-edge. The flow-induced noise is constantly very low because of the local low turbulence kinetic energy. Accordingly, different flow structures have different energy dissipation mechanisms. In this case, rotor-stator interaction affects both the internal energy and the flow-induced noise. The stalled vortex flow mainly causes the internal energy variation but weak in producing noise.
- (3) These high energy dissipation regions perform differently during rotor-stator interaction. Based on the frequency analysis, the transient characteristics of energy dissipation during impeller rotation can be clarified in detail. The flow regime on the diffuser blade leading-edge, on the diffuser blade's convex side and in the diffuser blade trailing-edge wake are influenced mainly by the impeller frequency or the impeller blade frequency. It shows that the rotor-stator interaction affects the flow regime, energy dissipation and flow-induced noise from diffuser inlet to outlet. The diffuser blade trailing-edge stall vortex is not strongly influenced by rotor-stator interaction. It keeps the stall frequency that is about 1/5 impeller frequency. This stall frequency also affects the diffuser trailing-edge wake region.

Generally, the energy dissipation in the centrifugal air pump is caused by local undesirable flow patterns. These local flow patterns are affected by rotor-stator interaction or stalled flow. Reducing energy dissipation is always the key in turbomachinery's optimization design. Therefore, understanding and quantifying the local energy dissipation can be helpful for the high-efficiency designs especially in the complex rotor-stator interacting flow cases.

Author Contributions: methodology, R.T. and X.Z.; investigation, R.T.; writing—original draft preparation, R.T. and X.Z.; writing—review and editing, X.Z. and Z.W.; supervision, Z.W.; project administration, R.T. and Z.W.; funding acquisition, R.T. and Z.W.

Funding: This research was funded by National Natural Science Foundation of China, grant number 51439002 and China Postdoctoral Science Foundation, grant number 2018M640126. The APC was funded by National Natural Science Foundation of China, grant number 51439002.

Conflicts of Interest: The authors declare no conflict of interest.

Nomenclature

Latin Letters

A_{in}	impeller inflow area	Q	flow rate
c_h	heat capacity	R_{cn}	Cone radius
C_k	turbulence kinetic energy coefficient	R_{d1}	Diffuser blade inlet radius
C_r	radial component of velocity	R_{d2}	Diffuser blade outlet radius
C_{stot}^*	energy dissipation coefficient	R_{hub}	Hub arc radius
C_t	tangential component of velocity	R_{i1}	Impeller blade inlet radius
C_{vrel}	relative velocity coefficient	R_{i2}	Impeller blade outlet radius
C_φ	flow rate coefficient	R_{in}	Impeller inflow radius
C_ω	production term coefficient in SST model	R_{shr}	Shroud arc radius
F_1	blending function in SST model	s^*	specific entropy
f_{ib}	impeller blade frequency	S_{ij}	strain tensor
f_{imp}	impeller frequency	S_p	spanwise position
f_{TEv}	diffuser trailing-edge stall frequency	t	time

g	acceleration of gravity	T	temperature
G_z	relative impeller blade channel position	T_{in}	temperature at inlet boundary
h_b	Height of impeller/diffuser blade	T_{out}	temperature at outlet boundary
h_{cn}	Height of cone	u	velocity
h_{hub}	Height over cone on hub	U_{i2}	Rotational linear speed at impeller outlet
h_{sta}	static enthalpy	V_c	sound speed
h_{tot}	total enthalpy	V_{in}	velocity at inlet boundary
k	turbulence kinetic energy	V_{out}	velocity at outlet boundary
$k-\omega$	turbulence scale in SST model	V_{rel}	relative velocity
L_{sp}	sound power level	W_A	sound power
M_t	specific turbulence kinetic energy	W_{ref}	reference sound power
n	Rotational speed	x	coordinate component
P	turbulence production term in SST model	y^+	dimensionless height off-wall
$P_1, P_2, P_3,$ P_4	monitoring point 1 to 4	Z_d	Diffuser blade number
p_{in}	pressure at inlet boundary	Z_i	Impeller blade number
p_{out}	pressure at outlet boundary		

Greek Letters

α_ε	model constant in acoustic analogy	μ_t	eddy viscosity
β_k	model constant in SST model	ρ	density
ΔC_{stot}	specific entropy difference coefficient	σ_k	model constant in SST model
δ_{ij}	Kroneker delta	σ_ω	model constant in SST model
ε	eddy dissipation rate	ϕ	denotation for arbitrary parameter in governing equations
λ_t	thermal conductivity	ω	specific turbulence dissipation rate
μ	dynamic viscosity		

Acronyms

CFD	computational fluid dynamics	LNR	low noise region
EXP	experiment	LVR	low C_{vrel} region
GGI	general grid interface	RANS	Reynolds-averaged Navier-Stokes
HKR	high k region	REV	impeller revolution
HNR	high noise region	RMS	root mean square
HVR	high C_{vrel} region	SS	blade suction side
LE	blade leading-edge	SST	shear stress transport
LKR	low k region	TE	blade trailing-edge

References

1. Çengel, Y.A.; Boles, M.A. *Thermodynamics an Engineering Approach*; McGraw-Hill: New York, NY, USA, 2015.
2. Zemansky, M.W. *Heat and Thermodynamics*; McGraw-Hill: New York, NY, USA, 1968.
3. Cattaert, A.E. High pressure pump efficiency determination from temperature and pressure measurements. In Proceedings of the Power Engineering Society Conference and Exposition in Africa, Johannesburg, South Africa, 16–20 July 2007.
4. Lavenda, B.H. *A New Perspective on Thermodynamics*; Springer: Berlin/Heidelberg, Germany, 2010.
5. Diaconescu, I. Analysis of irreversible thermodynamic processes from control valves. In Proceedings of the 3rd WSEAS International Conference on Energy Planning, Energy Saving, Environmental Education, Braila, Romania, 24–26 February 2009.
6. Esfahani, J.A.; Modirkhazeni, M.; Mohammadi, S. Accuracy analysis of predicted velocity profiles of laminar duct flow with entropy generation method. *Appl. Math. Mech.* **2013**, *34*, 971–984. [[CrossRef](#)]
7. Yoon, S.; Vandeputte, T.; Mistry, H.; Ong, J.; Stein, A. Loss audit of a turbine stage. In Proceedings of the ASME Turbo Expo 2015: Turbine Technical Conference and Exposition, Montreal, QC, Canada, 15–19 June 2015.
8. Jia, W.; Liu, H. Loss sources analysis of shroud leakage flow in highly-loaded turbine. *J. Propuls. Technol.* **2014**, *35*, 33–42.

9. VanZante, D.E.; To, W.M.; Chen, J.P. Blade row interaction effects on the performance of a moderately loaded NASA transonic compressor stage. In Proceedings of the ASME Turbo Expo 2002: Power for Land, Sea, and Air, Amsterdam, The Netherlands, 3–6 June 2002.
10. Liu, Z.H.; Shinji, M.; Miyagawa, K. Internal flow and loss mechanisms of specific speed 160 m-kW shroudless hydro turbine. *IOP Conf. Ser. Earth Environ. Sci.* **2018**, *163*, 012054. [[CrossRef](#)]
11. Sun, Y.; Ren, Y. Unsteady loss analyses of the flow in single-stage transonic compressor. *J. Tsinghua Univ. (Sci. Technol.)* **2009**, *49*, 759–762.
12. Li, D.; Gong, R.; Wang, H.; Xiang, G.; Wei, X.; Qin, D. Entropy production analysis for hump characteristics of a pump turbine model. *Chin. J. Mech. Eng.* **2016**, *29*, 803–812. [[CrossRef](#)]
13. Kluxen, R.; Behre, S.; Jeschke, P.; Guendogdu, Y. Loss mechanisms of interplatform steps in a 1.5-stage axial flow turbine. *J. Turbomach.* **2017**, *139*, 031007. [[CrossRef](#)]
14. Soltanmohamadi, R.; Lakzian, E. Improved design of wells turbine for wave energy conversion using entropy generation. *Meccanica* **2016**, *51*, 1713–1722. [[CrossRef](#)]
15. Zeinalpour, M.; Mazaheri, K. Entropy minimization in turbine cascade using continuous adjoint formulation. *Eng. Optim.* **2015**, *48*, 213–230. [[CrossRef](#)]
16. Acosta, A.J.; Brennen, C.E.; Caughey, T.K.; Caughey, T.K. Rotor-stator interaction in a diffuser pump. *Nat. Genet.* **1988**, *17*, 58–64.
17. Zhang, N.; Gao, B.; Li, Z.; Ni, D.; Jiang, Q. Unsteady flow structure and its evolution in a low specific speed centrifugal pump measured by PIV. *Exp. Therm. Fluid Sci.* **2018**, *97*, 133–144. [[CrossRef](#)]
18. Tao, R.; Xiao, R.; Liu, W. Investigation of the flow characteristics in a main nuclear power plant pump with eccentric impeller. *Nucl. Eng. Des.* **2018**, *327*, 70–81. [[CrossRef](#)]
19. Lighthill, M.J. On sound generated aerodynamically I: general theory. *Proc. R. Soc. Lond. (Ser. A)* **1952**, *211*, 564–587.
20. Langthjem, M.A.; Olhoff, N. A numerical study of flow-induced noise in a two-dimensional centrifugal pump. part I. hydrodynamics. *J. Fluids Struct.* **2004**, *19*, 349–368. [[CrossRef](#)]
21. Chen, M. *Fundamentals of Viscous Fluid Dynamics*; Higher Education Press: Beijing, China, 1993.
22. Terentiev, L. *The Turbulence Closure Model Based on Linear Anisotropy Invariant Analysis*; VDM Verlag: Saarbrücken, Germany, 2008.
23. Menter, F.R. Two-Equation Eddy-Viscosity Turbulence Models for Engineering Applications. *AIAA J.* **1994**, *32*, 1598–1605. [[CrossRef](#)]
24. Launder, B.E.; Spalding, D.B. The numerical computation of turbulent flows. *Comput. Methods Appl. Mech. Eng.* **1974**, *3*, 269–289. [[CrossRef](#)]
25. Wilcox, D.C. Formulation of the k- ω Turbulence Model Revisited. *AIAA J.* **2008**, *46*, 2823–2838. [[CrossRef](#)]
26. Proudman, I. The generation of noise by isotropic turbulence. *Proc. R. Soc. A* **1952**, *214*, 119–132.
27. Ubaldi, M.; Zunino, P.; Barigozzi, G.; Cattanel, A. An experimental investigation of stator induced unsteadiness on centrifugal impeller outflow. *J. Turbomach.* **1996**, *118*, 41–54. [[CrossRef](#)]
28. Bert, P.F.; Combès, J.F.; Kueny, J.L. Unsteady flow calculation in a centrifugal pump using a finite element method. In Proceedings of the XVIII IAHR Symposium on Hydraulic Machinery and Cavitation, Valencia, Spain, 16–19 September 1996.
29. Canepa, E.; Cattanei, A.; Ubaldi, M.; Zunino, P. Wake-boundary layer interaction on the vaned diffuser of a centrifugal state. *Proc. Inst. Mech. Eng. Part A J. Power Energy* **2005**, *219*, 401–411. [[CrossRef](#)]
30. Petit, P.; Nilsson, H. Numerical investigations of unsteady flow in a centrifugal pump with a vaned diffuser. *Int. J. Rotating Mach.* **2013**, *2013*, 961580. [[CrossRef](#)]
31. Huang, X.; Li, Y.; Liu, Z.; Yang, W. Numerical investigation of flow features in the vaneless region of a centrifugal pump by large eddy simulation. *Eng. Comput.* **2018**, *35*, 395–410. [[CrossRef](#)]
32. Zhao, X.; Wang, Z.; Xiao, Y.; Luo, Y. Thermodynamic analysis of energy dissipation and unsteady flow characteristic in a centrifugal dredge pump under over-load conditions. *Proc. Inst. Mech. Eng. Part C J. Mech. Eng. Sci.* **2019**, *2019*, 0954406218824350. [[CrossRef](#)]
33. Menter, F.R.; Esch, T. Elements of industrial heat transfer predictions. In Proceedings of the 16th Brazilian Congress of Mechanical Engineering, Minas Gerais, Brazil, 26–30 November 2001.
34. Cheng, A.H.-D.; Cheng, D.T. Heritage and early history of the boundary element method. *Eng. Anal. Bound. Elem.* **2005**, *29*, 268–302. [[CrossRef](#)]
35. Day, M.A. The no-slip condition of fluid dynamics. *Erkenntnis* **2004**, *33*, 285–296. [[CrossRef](#)]

36. Berten, S.; Dupont, P.; Fabre, L.; Kayal, M.; Avellan, F.; Farhat, M. Experimental investigation of flow instabilities and rotating stall in a high-energy centrifugal pump stage. In Proceedings of the ASME Fluids Engineering Division Summer Conference, Vail, CO, USA, 2–6 August 2009.
37. Wang, H.; Tsukamoto, H. Experimental and numerical study of unsteady flow in a diffuser pump at off-design conditions. *J. Fluids Eng.* **2003**, *125*, 767–778. [[CrossRef](#)]



© 2019 by the authors. Licensee MDPI, Basel, Switzerland. This article is an open access article distributed under the terms and conditions of the Creative Commons Attribution (CC BY) license (<http://creativecommons.org/licenses/by/4.0/>).